Hindawi
Computational Intelligence and Neuroscience
Volume 2021, Article ID 9528787, 10 pages
https://doi.org/10.1155/2021/9528787

Research Article

Parameter Measurement of Live Animals Based on the Mirror of Multiview Point Cloud

Jinsong Zhang, Yue Qin, and Li Wang

College of Communication and Electronic Engineering, Qiqihar University, Qiqihar 161006, China

Correspondence should be addressed to Jinsong Zhang; 01482@qqhru.edu.cn

Received 30 August 2021; Revised 13 October 2021; Accepted 13 October 2021; Published 29 October 2021

Academic Editor: Ahmed Mostafa Khalil

Scale and standardization are essential to the prosperity of the breeding industry. During large-scale, standardized breeding, the selective breeding of good livestock breeds hinges on the accurate measurement of body parameters for live animals. However, the complex shooting environment brings several urgent problems, such as the missing of many local data in the point cloud and the difficulty in the automatic acquisition of body data. To solve these problems, this paper proposes a method for parameter measurement of live animals based on the mirror of multiview point cloud. Firstly, the acquisition and stitching principles were given for the multiview point cloud data on body parameters of live animals. Next, the authors presented a way to make up for the data missing areas in the point cloud. Finally, this paper acquires the body mirror data of live animals and scientifically calculates the body parameters. The proposed measurement method was proved effective through experiments.

1. Introduction

Precision animal husbandry refers to the scientific breeding and management of live animals by arranging regular daily ration based on information technology. As an important aspect of intelligent agriculture, precision animal husbandry can improve the output benefit of animal husbandry products and ensure product quality and safety [1–4]. Large-scale, standardized breeding can effectively improve the output and profit of pigs, cattle, and sheep. During large-scale, standardized breeding, the selective breeding of good livestock breeds hinges on the accurate measurement of body parameters for live animals [5–12]. The manual measurements with tools like caliper and tap measure are greatly affected by subjective human factors. By contrast, the body measurement of three-dimensional (3D) body parameters, which cover the geometry of live animals, is relatively accurate. The measured data help to assess the health state of livestock, evaluate their body shapes, and identify their behavioral features [13–16].

Focusing on parameter measurement based on 3D point cloud data, Jo et al. [17] relied on the point cloud data of the 3D human body model to construct an objective interpolation function, which can describe the morphological changes of human body (e.g., gender, age, weight, height, and body proportion). Then, the independent elements were weighted reasonably according to the linkage been element changes. In this way, the independent elements were adjusted and updated. After that, the needed human body model was derived from the intermediate human body. Sato [18] proposed a hardware and software system capable of synchronization precise acquisition of point cloud data on live animals. The system consists of an FM810-GI depth camera and its fixation structure, a point cloud data processing module, and a repeater. Rao et al. [19] improved the stereo calibration method of point cloud data on live animals based on the location relationship between the multiple depth cameras used to collect the data. Then, the three-view point cloud data on live animals underwent stitching and duplicate removal by the interactive closest point (ICP) algorithm and k-means clustering (KMC). Finally, a precise 3D point cloud data was established for live animals.

To evaluate the health state of pandas, Turner et al. [20] introduced the skinned multianimal linear (SMAL) model to the 3D model reconstruction of these first class protected animals in China and obtained the base shape and base pose of the 3D panda model based on principal component

analysis (PCA) and bone movements. Further, they derived the parameterized description of the shape and pose of the model. Zhang et al. [21] manually extracted animal contours from two-dimensional (2D) images, set up the objective function of Euclidean clustering between SMAL model and contour segmentation maps, and estimated SMAL parameters by minimizing the objective function. Ahsan et al. [22] provided an effective and accurate way to measure the length, width, and depth of pavement cracks. Specifically, watershed segmentation was adopted to segment and mask the background of damaged pavement images, the coordinate system of pavement cracks was converted point by point, a 3D visual model was established on MATLAB for pavement cracks, and the computed results were compared with the measured data. To solve the precision product quality problems induced by manufacturing errors, Chen and Wang [23] proposed a 3D point cloud feature calculation method to compute the geometric and physical parameters of workpieces and combined area changes and centroid deviation into a dense layered part evaluation and adaptive stratification algorithm, which can reconstruct workpiece surfaces and adaptively stratify workpieces.

Some results have been achieved on 3D point cloud and body parameter extraction, as well as weight prediction [24–27]. However, there are often holes in the point cloud, owing to the complex environmental factors, e.g., environmental interference (especially the fences of the breeding base) and low equipment precision. These holes severely impede the postprocessing of the point cloud. In addition, it is very difficult to automatically acquire the body data of live animals [28–31]. To solve these problems, this paper proposes a method for parameter measurement of live animals based on the mirror of multiview point cloud. Section 2 introduces the acquisition and stitching principles of the multiview point cloud data on body parameters of live animals. Section 3 presents a way to make up for the data missing areas in the point cloud. Section 4 acquires the body mirror data of live animals and scientifically calculates the body parameters. The proposed measurement method was proved effective through experiments.

2. Data Acquisition and Stitching

During the 3D reconstruction of a specific object, the object must be extracted from the background to ensure the recognition and analysis accuracy. Owing to the complex environment of the breeding base, the point cloud data extracted from live animals contain the background, noises, and outliers. The data need to be preprocessed to remove the background and noises, facilitating further analysis. By visualizing the point cloud data of live animals, it is possible to obtain the left and right point cloud data of the background, including the ground, cameras, and noises. Considering the complex living environment of animals, the point cloud data were extracted from live animals in the following steps: (1) crop the point cloud data in the specified coordinate range, using passthrough filter; (2) remove ground point cloud data through planar template matching; and (3) eliminate outliers with redundant information by statistical filter.

Figure 1 shows the mirroring principle of multiview point cloud. It can be inferred that the multiview point cloud data on live animals contain multiple coordinate systems, such as rotation and translation. Point cloud registration is necessary to unify the coordinates of multiple point clouds under different coordinate systems.

Let G, p, and U be the rotation matrix, translation matrix, and perspective transform vector between two depth cameras, respectively, with U being a zero vector and $A = 1$ be the proportional factor of the multiview point cloud on live animals. Then, the mapping F of point cloud registration can be expressed as follows:

$$F = \begin{bmatrix} G_{11} & G_{11} & G_{11} & p \\ G_{21} & G_{22} & G_{23} & p \\ G_{31} & G_{32} & G_{33} & p \\ u_x & u_y & u_s & A \end{bmatrix} \longrightarrow F = \begin{bmatrix} G_{3\times3} & p_{3\times1} \\ U_{1\times3} & A \end{bmatrix}. \tag{1}$$

To directly stitch point clouds on live animals, it is necessary to determine the location relationship between depth cameras. The parameters can be obtained through the stereo calibration in the binocular visual system. Let O_{SJ} be the coordinate of any point O in the world coordinate system; G_1 and G_2 be the rotation matrices of cameras 1 and 2 relative to the calibration object, respectively; and p_1 and p_2 be the translation matrices of cameras 1 and 2 relative to the calibration object, respectively. Under the world coordinate system, the coordinates of the two cameras can be described by the following:

$$\begin{cases} O_1 = G_1 O_{SJ} + p_1, \\ O_2 = G_2 O_{SJ} + p_2. \end{cases} \tag{2}$$

The relationship between O_1 and O_2 can be established as follows:

$$O_1 = GO_2 + p. \tag{3}$$

Combing formulas (2) and (3),

$$\begin{cases} G = G_1 (G_2) p, \\ p = p_1 - G p_2. \end{cases} \tag{4}$$

According to the affine invariance of four point pairs in 4-point congruent sets (4PCS), the distance ratio g can be fixed with three known colinear points U, V, and W:

$$g = \left\| \frac{U - V}{U - W} \right\|. \tag{5}$$

Suppose U and W fall on the same straight line and V and Q fall on the same straight line. In addition, the two lines intersect at point H. Then, distance ratios g_1 and g_2 can be calculated by the following:

$$\begin{aligned} g_1 &= \left\| \frac{U - H}{U - W} \right\|, \\ g_2 &= \left\| \frac{V - H}{V - Q} \right\|. \end{aligned} \tag{6}$$

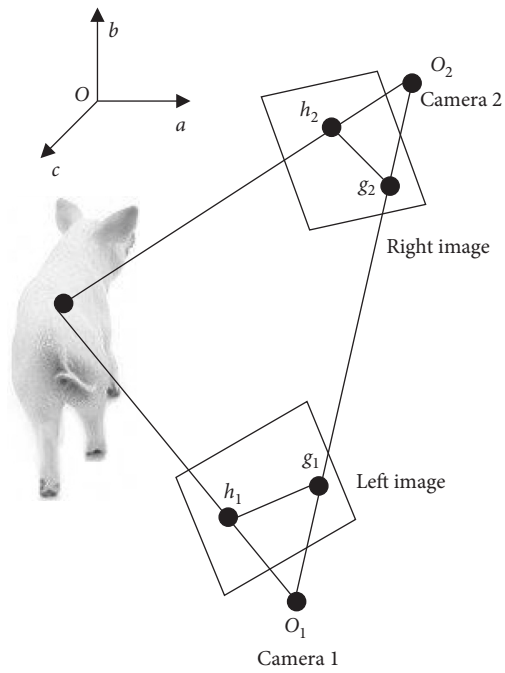

Figure 1: Mirroring principle of multiview point cloud.

During affine transform, the distance ratios g_1 and g_2 determined by the four coplanar points of the source point cloud and the corresponding four points in the target point cloud are constant, i.e., completely the same. If there exists any point pair s_1 and s_2 in S whose lines intersect at points h_1 and h_2, which are the same within a certain error range, then s_1 and s_2 are the coplanar points corresponding to the given base in the world coordinate system. The intersections h_1 and h_2 can be calculated by the following:

$$\begin{aligned} h_1 &= s_1 + g_1(s_2 - s_1), \\ h_2 &= s_1 + g_2(s_2 - s_1). \end{aligned} \tag{7}$$

If the point cloud data on live animals are stitched directly using the results of stereo calibration, the registration accuracy needs to be guaranteed through iterations by the precision matching algorithm *ICP*. Suppose the point set under the world coordinate system and the target point set is denoted as $O = \{o_i | o_i \in \mathbb{R}^3,\ i = 1, 2, \ldots, m\}$ and $S = \{s_j | s_j \in \mathbb{R}^3,\ j = 1,2, \ldots, n\}$, respectively. Under the premise of minimizing the error function error(G, p) between the two point sets in formula (8), the least squares method can be adopted to iteratively perform the optimal coordinate transform and calculate the rotation matrix and translation matrix until the preset error threshold or maximum number of iterations is reached:

$$\text{error}(G, p) = \frac{1}{m} \sum_{i=1}^{m} \left\| s_i - (Go_i + p) \right\|^2. \tag{8}$$

3. Repairing Missing Areas

To make up for the large nonclosed missing areas in the point cloud of live animals, this paper proposes the cubic B-spline curve fitting method based on the projections of point cloud slices.

The slicing of the point cloud on live animals was carried out along the a-axis. The first step is to determine the minimum distance $\varepsilon_{\min}$ between the point cloud center and other points and the maximum $a_{\max}$ and minimum $a_{\min}$ of the center along the a-axis. Next, point cloud splices were sampled from $a_{\min}$ in the positive direction of a-axis, with an interval of $\varepsilon_{\min}$. The sampling number M_S can be calculated by the following:

$$M_S = \lceil \frac{a_{\max} - a_{\min}}{\varepsilon_{\min}} \rceil, \tag{9}$$

where the square brackets stand for rounding operation. The sampling interval of the i-th point cloud slice O_i can be described as $[a_{\min} + (i-1)\ \varepsilon_{\min},\ a_{\min} + i\varepsilon_{\min}]$. Then, the maximum $b_{i-\max}$ and minimum $b_{i-\min}$ of O_i along b-axis were determined, and the point cloud was sliced into M_i parts with an interval of $\varepsilon_{\min}$:

$$M_i = \lceil \frac{b_{i-\max} - a_{i-\min}}{\varepsilon_{\min}} \rceil. \tag{10}$$

The curve fitting effect is greatly affected by the number of new points appearing through the expansion of the interval of point cloud slices. Therefore, this paper selects the center O_{il} of the l-th interval $[b_{i-\min} + (l-1)\ \varepsilon_{\min},\ b_{i-\min} + l\ \varepsilon_{\min}]$ of O_i long b-axis as the representative point of that interval. Suppose the interval contains N_l points, with O_{ilk} being the k-th point. Then, we have

$$O_{il} = \frac{1}{N_l} \sum_{j=1}^{N_l} O_{ilk}. \tag{11}$$

The processed O_i was projected onto plane boc. The projection point was then fitted. When restoring the fitted point cloud O_i^* to the space, the points in interval O_i^* along a-axis should be configured uniformly:

$$a_i^* = a_{\min} + \left(p - \frac{1}{2} \right) \cdot \varepsilon_{\min}. \tag{12}$$

Suppose the slice plane or space of the point cloud on live animals contains $u + v + 1$ vertices. Then, O_i has a v-dimensional parametric curve segment:

$$O_{jv}(p) = \sum_{j=0}^{u} O_{j+l} R_{j,v}(p). \tag{13}$$

The v-dimensional B-spline curve can be derived from the v-dimensional B-spline curve segment $O_{jv}(p)$ above. The base function $R_{iv}(p)$ of the curve can be calculated by the following:

$$R_{iv}(p) = \frac{1}{v!} \sum_{t=0}^{v-t} (-1)^t W_{v+1}^t (p + v - i - t)^v. \tag{14}$$

The v-dimensional B-spline curve can be defined by $v - 1$ adjacent vertices. Then, the cubic B-spline curve can be expressed as follows:

$$O_{j3}(p) = \sum_{i=0}^{3} O_{i+j} R_{i,3}(p). \quad (15)$$

The corresponding base function can be expressed as follows:

$$\begin{cases} R_{0,3}(p) = \frac{1}{6}\left(-p^3 + 3p^2 - 3p + 1\right), \\ R_{1,3}(p) = \frac{1}{6}\left(3p^3 - 6p^2 + 4\right), \\ R_{2,3}(p) = \frac{1}{6}\left(-3p^3 + 3p^2 + 3p + 1\right), \\ R_{3,3}(p) = \frac{1}{6}p^3. \end{cases} \quad (16)$$

The j-th segment of the cubic B-spline curve can be described by the following:

$$O_{j3}(p) = \frac{1}{6}\begin{bmatrix} 1 & p & p^2 & p^3 \end{bmatrix}\begin{bmatrix} 1 & 4 & 1 & 0 \\ -3 & 0 & 3 & 0 \\ 3 & -6 & 3 & 0 \\ -1 & 3 & -3 & 1 \end{bmatrix}\begin{bmatrix} O_j \\ O_{j+1} \\ O_{j+2} \\ O_{j+3} \end{bmatrix}. \quad (17)$$

Figure 2 shows the projection and fitting of point cloud slices on the forelimbs of a cow. After the projection and fitting, the distance between adjacent points averaged at 6.842 mm, the standard deviation was 1.514 mm, and the approximate error was 0.426 mm. The number of points increased by 67.2% to 270. The fitted range of points was close to the original range of points.

4. Mirror Data Acquisition and Parameter Calculation

4.1. Key Point Positioning and Mirror Data Acquisition. Figure 3 presents the side view of a live animal. To obtain the exact values of the body parameters, it is necessary to locate the key points of the body of the live animal. Cattle, pigs, and sheep share the same key points, including the point of maximum abdominal width, the shoulder point and its transition points, the point of ischial tuberosity, and the point of withers.

During the preprocessing, the ground plane equation was defined for each frame of the point cloud. The side view and top view correspond to planes aob and aoc, respectively. Specifically, the point of maximum abdominal width P_1 is the point furthest away from the line connecting the left and right end points in the fitted point range. The transition point P_2 of the shoulder point P_4 characterizes the point at which the slope of the cloud segment P_1–P_4 turns from positive to negative. Along the positive direction of axis a, the number M_{EK} of centers in the cloud segment P_1–P_4 was

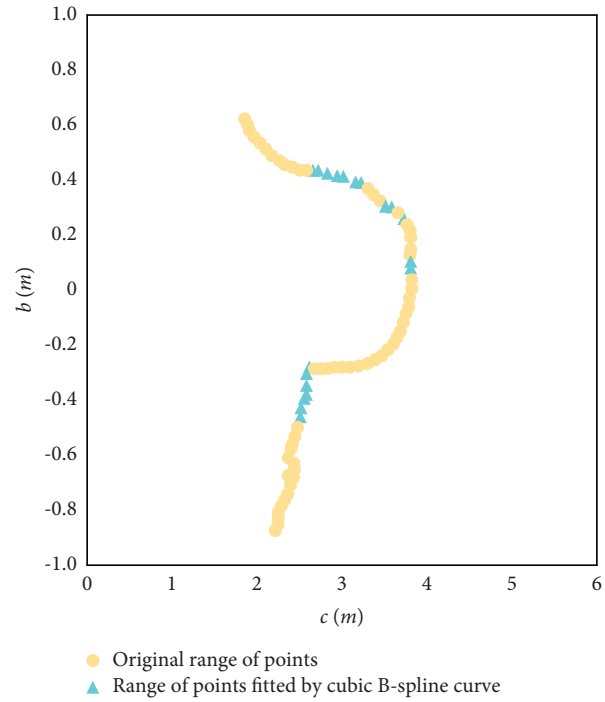

Figure 2: Projection and fitting of point cloud slices on forelimbs of live animals.

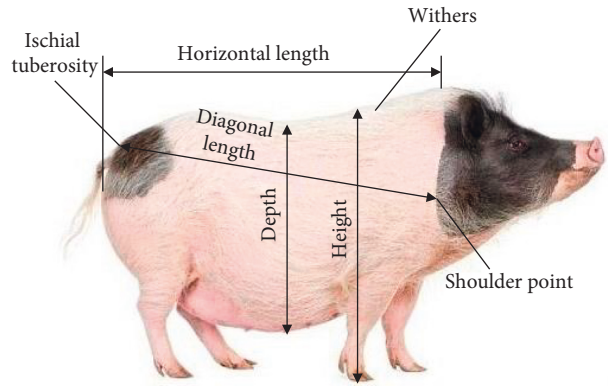

Figure 3: Side view of a live animal.

calculated with P_1 (a_1, c_1) as the starting point. Then, the angle ω_i between axis a and the line connecting P_1 with each point in O_i (a_o, c_o) ($i = 1,2, \ldots, M_{EK}$) can be calculated by the following:

$$\omega_i = \arctan\left|\frac{c_{o_i} - c_1}{a_{o_i} - a_1}\right|. \quad (18)$$

The nearby transition point P_3 at which the slope also turns from positive to negative was identified in a similar manner as point P_2. Along the positive direction of axis a, the number MFK of centers in the cloud segment P_1–P_4 was calculated with P_2 (a_2, c_2) as the starting point. Then, the angle ω_j between axis a and each point in O_i (a_o, c_o) ($i = 1,2, \ldots,$ MFK) with P_1 (a_1, c_1) as the starting point and satisfying $c_{oj} \geq c_1$ can be obtained by the following:

$$\begin{cases} a_1 = a_{c_{\min}}, c_1 = \dfrac{c_{\min} + c_{\max}}{2}, \\ \omega_j = \arctan\left|\dfrac{c_{o_i} - c_1}{a_{o_i} - a_1}\right|, \\ c_{p_i} \geq c_1. \end{cases} \tag{19}$$

After obtaining P_2 and P_3, the shoulder point of the live animal P_4 was determined as the farthest point in the point cloud segment P_2-P_3 from the line connecting P_2 and P_3. Then, the point of ischial tuberosity P_5 could be obtained as the center of the K nearest points to the point of minimum a. After that, the point of withers P_6 could be solved by computing the center coordinates of all the tallest points in the 2 slice point clouds extended to the left and right of the axis a coordinates of the midpoint of P_2 and P_4. Finally, the upper point P_U and lower point P_D of the depth could be solved by computing the center coordinates of all the tallest points and all the lowest points in the 2 slice point clouds extended to the left and right of the axis a coordinates of point P_1, respectively.

To get an accurate plane of symmetry for the body of the live animal, the normal vector γ_{op} of the ground supporting the animal and the horizontal direction vector ξ_p of the animal were aligned with the positive directions of axes a and b, respectively, to normalize the poses. Then, the normal vector ϕ_p of the plane of symmetry is the product between γ_{op} and ξ_p:

$$\varphi_p = \gamma_{op} \times \xi_p. \tag{20}$$

The above analysis shows that the tail point of the live animal is the extreme point in the negative direction of axis a, whose coordinates are (a_0, b_0, c_0). From (a_0, b_0, c_0) and ϕ_p, the planar equation of the live animal can be determined as $c = c_0$. The mirror data on one side of the plane of asymmetry could be obtained by setting up the homogeneous coordinates of the point $O_{t1} = \{(a, b, c)|c > c_0\}$ on one side of the plane:

$$\begin{bmatrix} a' & b' & c' & 1 \end{bmatrix} = \begin{bmatrix} a & b & c & 1 \end{bmatrix} \begin{bmatrix} 1 & 1 & 1 & 0 \\ 0 & 1 & 0 & 0 \\ 0 & 0 & -1 & 0 \\ 0 & 0 & 2c_0 & 1 \end{bmatrix}. \tag{21}$$

After obtaining the symmetric data $O_{t2} = \{(a', b', b'|a', b', c \in O_{t2}\}$ of the live animal, it is assumed that $O_t = O_{t1} + O_{t2}$, where O_t is the mirror of the point cloud on the complete animal in the 3D space.

4.2. Calculation of Body Parameters. The Euclidean distance from $P_4(a_4, b_4, c_4)$ to $P_5(a_5, b_5, c_5)$ was defined as the diagonal length of the Euclidean distance:

$$\zeta_O = \sqrt{(a_4 - a_5)^2 + (b_4 - b_5)^2 + (c_4 - c_5)^2}. \tag{22}$$

The horizontal distance from P_4 (a_4, b_4, c_4) to the vertical line of P_5 (a_5, b_5, c_5) was defined as the horizontal distance:

$$\zeta_S = |a_4 - a_5|. \tag{23}$$

The shoulder width was defined as twice the distance from $P_4(a_4, b_4, c_4)$ to the plane of symmetry $c = \mu_0^* + \mu_1 a$:

$$\psi_J = \frac{|\mu_1 a_4 - c_4 + \mu_0^*|}{\sqrt{\mu_1^2 + 1}}. \tag{24}$$

The abdominal width was defined as twice the distance from P_1 (a_1, b_1, c_1) to $c = \mu_0^* + \mu_1 a$:

$$\psi_F = \frac{|\mu_1 a_5 - c_5 + \mu_0^*|}{\sqrt{\mu_1^2 + 1}}. \tag{25}$$

The height was defined as the distance from P_6 (a_6, b_6, c_6) to the ground $\tau_a a + \tau_b b + \tau_c c + \upsilon = 0$:

$$H_A = \frac{|\tau_a a_6 + \tau_b b_6 + \tau_c c_6 + \upsilon|}{\sqrt{\tau_a^2 + \tau_b^2 + \tau_c^2}}. \tag{26}$$

The depth was defined by the vertical heights of P_U $(a^P{}_U, b^P{}_U, c^P{}_U)$ and P_D $(a^P{}_D, b^P{}_D, c^P{}_D)$:

$$T_{u,v} = |c_{P_U} - c_{P_D}|. \tag{27}$$

5. Experiments and Result Analysis

During the acquisition of point cloud data from live animals, it is difficult to shoot an image and complete 3D calibration using normal calibration targets. Thus, this paper performs 3D calibration with large and small infrared calibration targets. Depending on the deployment of depth cameras, the overhead camera was calibrated separately with the left infrared lens of the left camera and the right infrared lens of the right camera. The calibration errors are recorded in Figures 4(a) and 4(b). It can be inferred that the mean reprojection error between overhead camera and the left infrared lens of right camera was 1.31 pixels, and that between overhead camera and the right infrared lens of left camera was 0.87 pixels. Both results meet the precision requirements.

The axis a coordinates of chest circumference measuring points on a live pig were recorded on interactive measuring software of point cloud data. The fitting parameters were set as follows: the order of the curve, 4; the number of iterations, 50; and the number of control points, 100. Figure 5(a) shows the point cloud within 0.005 before and after the coordinates obtained by passthrough filter. Figure 5(b) shows the curve obtained by our cubic B-spline curve fitting method, which is marked in red. The curve circumference could be estimated from the length of the approximate polygon composed of the curve control points.

Our point cloud repairing method was applied to the missing areas in the 240 frames of point clouds on 50 pigs. These areas went missing due to the occlusions of railings. The fitting errors of the traditional method and our method

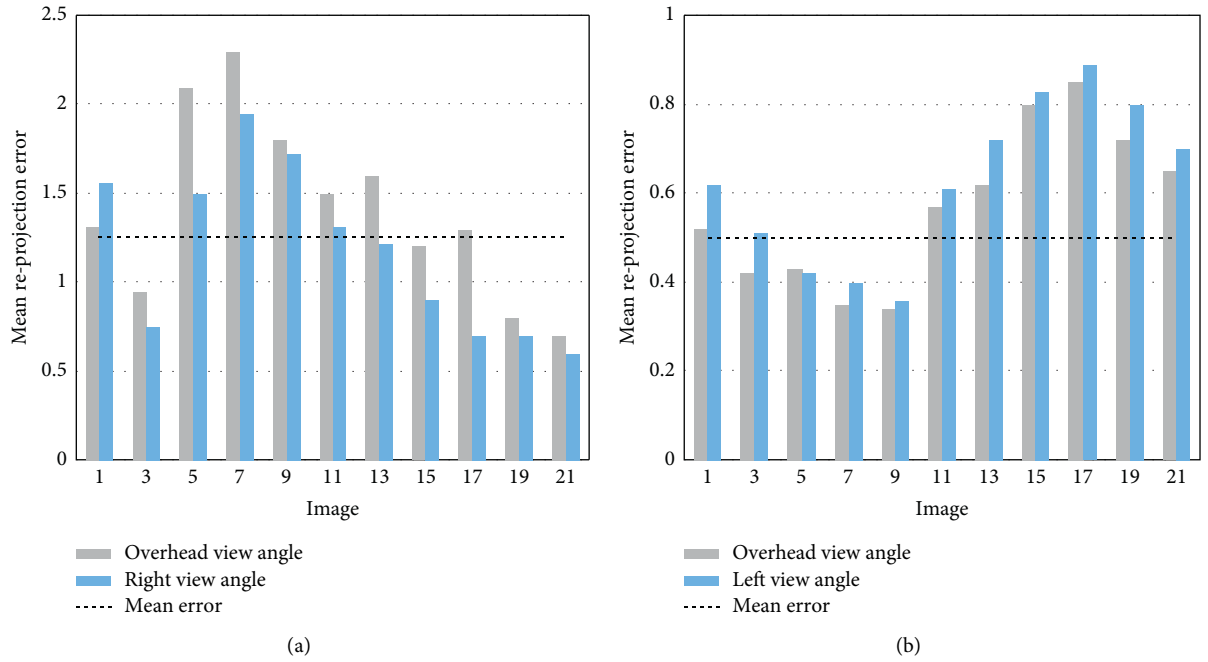

Figure 4: Mean reprojection errors of overhead, left, and right depth cameras: (a) overhead and right cameras; (b) overhead and left cameras.

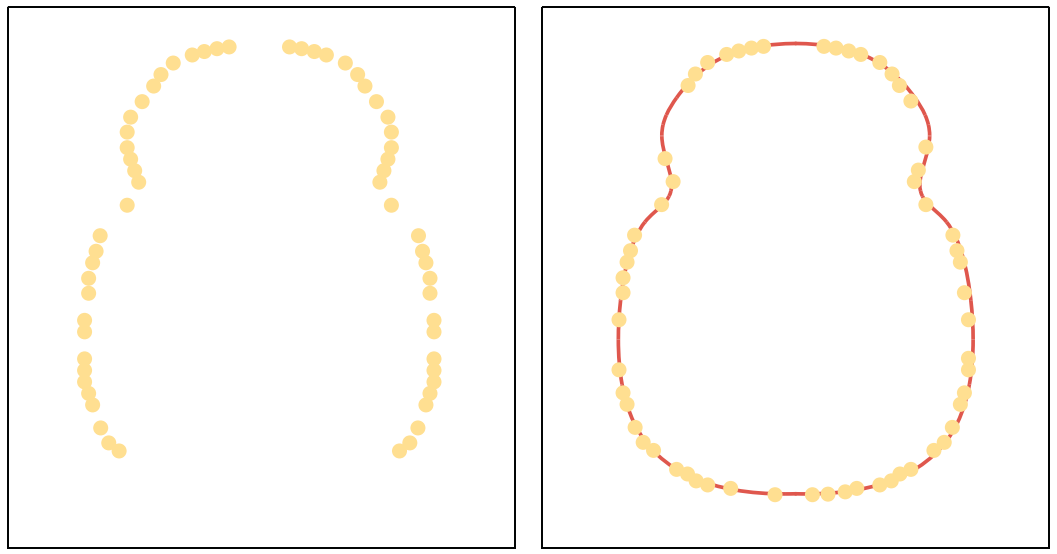

Figure 5: Curves fitted from chest circumference measuring points: (a) passthrough filter; (b) our method.

are displayed in Figure 6. The mean, maximum, and minimum fitting errors of traditional cubic B-spline curve were 2.524 mm, 4.452 mm, and 2.346 mm, respectively; those of our method, i.e., cubic B-spline curve fitting based on projection of point cloud slices, were 1.924 mm, 3.754 mm, and 1.859 mm, respectively. This further confirms that the curve fitted by our method is closer to the original point cloud.

To verify its effectiveness, the proposed algorithm was compared with two other models through experiments. The processing results of different models are listed in Table 1. Our algorithm achieved relatively good results on segmenting live animals in point cloud data: the recall was as high as 82.7% and the accuracy as 88.9%. The recall and accuracy of region growth + threshold judgement were 80.4% and 82.7%, respectively. The recall and accuracy of watershed segmentation were merely 55.1% and 80.4%, respectively. The comparison shows that our algorithm boasts a good precision and high recall and accuracy. As for the two contrastive models, region growth + threshold

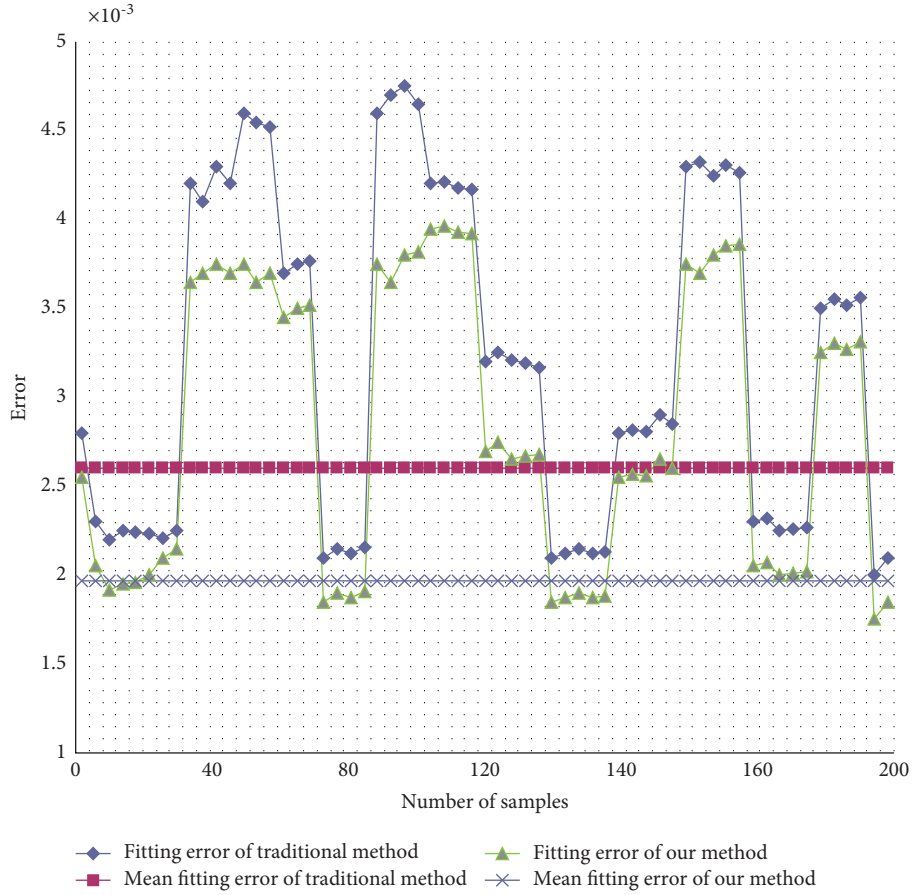

Figure 6: Errors of different methods in missing area repairing.

Table 1: Processing results of different models.

Model	Live animals	Number of samples	Number of effectively segmented samples	Number of oversegmented samples	Number of undersegmented samples	Recall	Accuracy
Watershed segmentation	Pigs	154	87	15	34	55.1	77.1
	Cattle	227	103	22	29	54.3	80.4
Region growth + threshold judgement	Pigs	154	99	14	31	67.8	81.4
	Cattle	227	134	21	22	80.4	82.7
Our algorithm	Pigs	154	139	14	30	74.2	88.9
	Cattle	227	188	20	21	82.7	83.7

judgement outperformed watershed segmentation in both recall and accuracy.

The body appearance of live animals can be well displayed by the side view captured by depth cameras and characterized by the projection of point range on plane aoc. In general, the local curves of the projected point range are not smooth enough despite being relatively simple. The local point range could be fitted ideally, using a cubic polynomial in one variable with 2 extremes. The fitting effect is shown in Figure 7(a). The key points of live animal body are presented in Figure 7(b), including the point of maximum abdominal width P_1, the shoulder point P_4 and its transition points P_2 and P_3, and the point of ischial tuberosity P_5. The positions of the point cloud on the live animal projected to the 3D space could be derived from the projected position of each of these points.

The point cloud data obtained from one side only cover half of the body of the live animal. This calls for the restoration of the mirror of the point cloud. After determining the symmetric longitudinal section along the line connecting the center of the head and the center of the tail of the live animal, the shoulder width is equivalent to twice the distance from the point of maximum shoulder width to the plane of symmetry. Similarly, the abdominal width is equivalent to twice the distance from the point of maximum abdominal width to the plane of symmetry. The tallest points on the

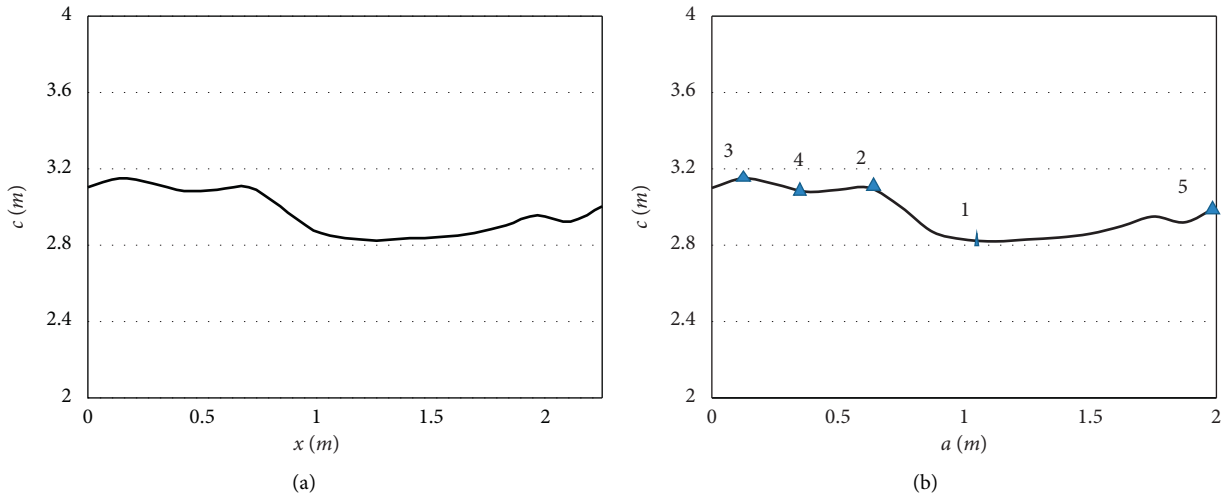

Figure 7: (a) Point range projection. (b) Key point identification.

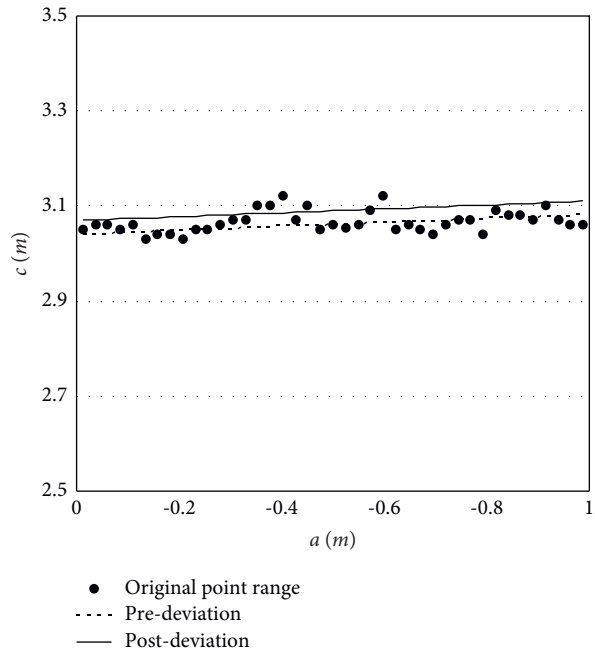

Figure 8: Fitted line of symmetry.

point cloud slices between the following points were merged into a point range: point of maximum abdominal width P_1, shoulder point P_4 and its transition points P_2 and P_3, and point of ischial tuberosity P_5. Then, the outliers were removed from the point range, and the center coordinates were solved. The resulting new point range was fitted by a linear equation. Then, the straight line was translated to the mean distance from every point in the range to the center coordinates, producing the line of symmetry of the live animal. Then, it is possible to derive the mirror data of the point cloud of that animal. Figure 8 shows the fitted line of symmetry.

The body parameters were extracted and measured from the 240 frames of point clouds on 50 pigs. Table 1 presents the measured results. Table 2 compares the point cloud measurements with manual measurements.

As shown in Table 3, the MAE of height measurement was minimized at 0.0032. The MAEs of other parameters were within 0.0270. Specifically, diagonal length and horizontal length had relatively large MAEs (0.0262 and 0.0232), 35% greater than the MAEs of other parameters. The MRE of height was also minimized at 0.9127%. The MRE of horizontal length was 5.0327, above the MREs of all the other five parameters. Regardless of MAE or MRE, the measurement errors of horizontal and diagonal lengths were relatively large, while those of height and depth were small. The main reason is that the slight changes of body position of the live animals during the measurement affects the accuracy of key

Table 2: Measured results of body parameters.

Serial number	Diagonal length	Horizontal length	Shoulder width	Abdominal width	Height	Depth
1	1.6335	1.6312	0.3125	0.7802	1.4125	0.7936
2	1.8203	1.7536	0.5327	0.8231	1.4257	0.8752
3	1.5721	1.5264	0.5346	0.7523	1.4329	0.8534
4	1.3592	1.6317	0.6371	0.6375	1.3546	0.7580
5	1.6317	1.7322	0.3511	0.7438	1.4728	0.8375
6	1.7692	1.7605	0.3670	0.6782	1.4159	0.8351
7	1.7326	1.5632	0.5234	0.9357	1.3072	0.8439
8	1.6545	1.4725	0.5602	0.7521	1.3821	0.8217
9	1.5217	1.6241	0.5437	0.6325	1.5057	0.7536
10	1.6039	1.5492	0.6539	0.7253	1.3723	0.8419

Table 3: Measurement errors.

	Diagonal length	Horizontal length	Shoulder width	Abdominal width	Height	Depth
Mean absolute error (MAE)	0.0262	0.0232	0.0193	0.0185	0.0032	0.0096
Mean relative error (MRE)	4.9235	5.0327	3.9752	2.4371	0.9127	1.1358

point identification. Besides, the subjectiveness of manual measurement also influences the determination of key points. Of course, the errors were relatively small. The above results show that our measurement method for body parameters is accurate enough for application.

6. Conclusions

This paper develops a parameter measurement method for live animals based on the mirror of multiview point cloud. After being acquired from the target animal, the point cloud data from multiple views were preprocessed and stitched, followed by the eliminating of redundant background points. Next, the features of the point cloud data were analyzed, and a 3D point cloud data model was established for live animals. After that, the authors explained how to repair the missing part of the point cloud data, acquired the mirror data on animal body, and scientifically computed the body parameters. Experimental results confirm the scientific nature of the calibrating overhead camera separately with the left infrared lens of the right camera and the right infrared lens of the left camera. In addition, the chest circumference measuring points were fitted into a curve, and the errors of different methods were compared for repairing missing areas in the point cloud. The relevant results demonstrate the effectiveness of our fitting algorithm. Further, the line of asymmetry of a live animal was fitted, which proves the feasibility and effectiveness of our point cloud acquisition method. Finally, the measuring errors of body parameters were presented, suggesting the high accuracy of our body parameter measuring method for live animals.

Data Availability

The data used to support the findings of this study are available from the corresponding author upon request.

Conflicts of Interest

The authors declare that they have no conflicts of interest regarding the publication of this paper.

Acknowledgments

This study was supported by Research Program supported by Basic Research Operating Expenses for Provincial Institutions of Higher Learning, Heilongjiang Province, China (Grant No. 135309457).

References

[1] N. Senin, S. Catalucci, M. Moretti, and R. K. Leach, "Statistical point cloud model to investigate measurement uncertainty in coordinate metrology," *Precision Engineering*, vol. 70, pp. 44–62, 2021.

[2] P. Rattanasuwan, I. Kumazawa, and T. Kasetkasem, "Non-destructive measurement of rice leaf dimension in 3D point cloud," *IOP Conference Series: Earth and Environmental Science*, vol. 633, no. 1, p. 012013, 2021.

[3] J. Walczak and A. Wojciechowski, "Clustering quality measures for point cloud segmentation tasks," in *Proceedings of the International Conference on Computer Vision and Graphics*, pp. 173–186, Warsaw, Poland, September 2018.

[4] A. Dineva, A. R. Várkonyi-Kóczy, V. Piuri, and J. K. Tar, "Point cloud processing with the combination of fuzzy information measure and wavelets," in *Proceedings of the International Workshop Soft Computing Applications*, pp. 455–461, Arad, Romania, August 2016.

[5] H. Guo, Z. Li, Q. Ma et al., "A bilateral symmetry based pose normalization framework applied to livestock body measurement in point clouds," *Computers and Electronics in Agriculture*, vol. 160, pp. 59–70, 2019.

[6] T. Satoh, T. Yotsumata, and K. Mano, "New technology on 3d point cloud by laser measurement of various platforms," *Journal of the Japan Society for Precision Engineering*, vol. 85, no. 3, pp. 223–227, 2019.

[7] L. B. Zhang, D. Wu, H. Y. Shan, and Q. F. Liu, "Dynamic measurement method for vehicle contour dimensions based on laser point cloud," *Huanan Ligong Daxue Xuebao/Journal of South China University of Technology (Natural Science)*, vol. 47, no. 3, pp. 61–69, 2019.

[8] R. J. L. Hartley, E. M. Leonardo, P. Massam et al., "An assessment of high-density UAV point clouds for the

measurement of young forestry trials," *Remote Sensing*, vol. 12, no. 24, Article ID 4039, 2020.

[9] S. J. Ray and J. Teizer, "Computing 3D blind spots of construction equipment: implementation and evaluation of an automated measurement and visualization method utilizing range point cloud data," *Automation in Construction*, vol. 36, pp. 95–107, 2013.

[10] E. Srichandra and V. Sangveraphunsiri, *A Point Cloud Interpolation Technique for Enhancing Measurement of A 3-D Coordinate Measuring Machine*, Acta Press, Calgary, Canada, 2013.

[11] H. Soltani Panah, A. Haghtalab, M. Abdollahi et al., "Experimental measurements and thermodynamic modeling of the cloud point pressure for solubility of copolymers of vinyl acetate and dibutyl maleate in supercritical CO2," *Fluid Phase Equilibria*, vol. 425, pp. 136–142, 2016.

[12] N. Namitha, S. M. Vaitheeswaran, V. K. Jayasree, and M. K. Bharat, "Point cloud mapping measurements using kinect RGB-D sensor and kinect fusion for visual odometry," *Procedia Computer Science*, vol. 89, pp. 209–212, 2016.

[13] B. Zeise and B. Wagner, "Tempered point clouds and octomaps: a step towards true 3D temperature measurement in unknown environments," in *Proceedings of the2017 IEEE International Symposium on Safety, Security and Rescue Robotics (SSRR)*, pp. 88–95, Shanghai, China, October 2017.

[14] M. A. Rahim, S. Mahbub, M. K. Islam et al., "Influence of different additives on the interaction of quinolone antibiotic drug with surfactant: conductivity and cloud point measurement study," *Journal of Surfactants and Detergents*, vol. 23, no. 2, pp. 457–470, 2020.

[15] A. Saglam, H. B. Makineci, Ö. K. Baykan, and N. A. Baykan, "Clustering-based plane refitting of non-planar patches for voxel-based 3D point cloud segmentation using k-means clustering," *Traitement du Signal*, vol. 37, no. 6, pp. 1019–1027, 2020.

[16] G. Q. Ma, L. Liu, Z. L. Yu, G. H. Cao, and Q. Wang, "Ointcloud splicing technology for large-scale surface topography measurement system," *Zhongguo Jiguang/Chinese Journal of Lasers*, vol. 46, no. 5, 2019.

[17] H. C. Jo, J. Kim, K. Lee, H.-G. Sohn, and Y. M. Lim, "Noncontact strain measurement for laterally loaded steel plate using LiDAR point cloud displacement data," *Sensors and Actuators A: Physical*, vol. 283, pp. 362–374, 2018.

[18] O. Sato, "ABC's of measurement point cloud validation against 3D-CAD data," *Journal of the Japan Society for Precision Engineering*, vol. 84, no. 9, pp. 782–784, 2018.

[19] G. Rao, G. Wang, X. Yang, J. Xu, and K. Chen, "Normal direction measurement and optimization with a dense three-dimensional point cloud in robotic drilling," *IEEE/ASME Transactions on Mechatronics*, vol. 23, no. 3, pp. 986–996, 2017.

[20] A. P. Turner, J. J. Jackson, N. K. Koeninger et al., "Stored grain volume MeasurementUsing a low density point cloud," *Applied Engineering in Agriculture*, vol. 33, no. 1, pp. 105–112, 2017.

[21] X. Y. Zhang, G. Liu, L. Jing, Y. S. Si, X. H. Ren, and L. Ma, "Automatic extraction method of cow's back body measuring point based on simplification point cloud," *Transactions of the Chinese Society for Agricultural Machinery*, vol. 50, pp. 267–275, 2019.

[22] S. M. A. Ahsan, M. R. Molla, M. S. Rahman et al., "Investigation of the interaction of levofloxacin hemihydrate with surfactants in the occurrence of salts: conductivity and cloud point measurement," *Journal of Molecular Liquids*, vol. 274, pp. 484–496, 2019.

[23] X. Chen and J. Wang, "Breast volume measurement by mesh projection method based on 3D point cloud data," *International Journal of Clothing Science & Technology*, vol. 27, no. 2, pp. 221–236, 2015.

[24] Y. Ge, H. Tang, D. Xia et al., "Automated measurements of discontinuity geometric properties from a 3D-point cloud based on a modified region growing algorithm," *Engineering Geology*, vol. 242, pp. 44–54, 2018.

[25] F. C. Jiang, H. Y. Zhang, and C. Zhu, "Three-dimensional target detection based on RGB-D data," *Traitement du Signal*, vol. 38, no. 2, pp. 315–320, 2020.

[26] P. K. Rao, Z. Kong, C. E. Duty, and R. J. Smith, "Three dimensional point cloud measurement based dimensional integrity assessment for additive manufactured parts using spectral graph theory," in *Proceedings of the International Manufacturing Science and Engineering Conference*, Blacksburg, VA, USA, September 2016.

[27] E. Özbay and A. Çınar, "A comparative study of object classification methods using 3D Zernike moment on 3D point clouds," *Traitement du Signal*, vol. 36, no. 6, pp. 549–555, 2019.

[28] M. Wang, S. Harrisson, M. Destarac, and J. D. Marty, "Measuring cloud point pressures by image analysis: a simple and reproducible alternative method to direct visual determination," *The Journal of Supercritical Fluids*, vol. 152, Article ID 104572, 2019.

[29] Z. Peng, "An operation and maintenance strategy of intelligent building information model data based on cloud computing," *Ingénierie des Systèmes d'Information*, vol. 25, no. 4, pp. 461–467, 2020.

[30] L. Saba, S. K. Banchhor, H. S. Suri et al., "Accurate cloud-based smart IMT measurement, its validation and stroke risk stratification in carotid ultrasound: a web-based point-of-care tool for multicenter clinical trial," *Computers in Biology and Medicine*, vol. 75, pp. 217–234, 2016.

[31] F. Zhang, C. Zhang, H. Yang, and L. Zhao, "Point cloud denoising with principal component analysis and a novel bilateral filter," *Traitement du Signal*, vol. 36, no. 5, pp. 393–398, 2019.